ACS APPLIED MATERIALS & INTERFACES

Research Article

www.acsami.org

Aerosol-Assisted Chemical Vapor Deposition of Tungsten Oxide Films and Nanorods from Oxo Tungsten(VI) Fluoroalkoxide Precursors

Hankook Kim,[†] Richard O. Bonsu,[‡] Christopher O'Donohue,[†] Roman Y. Korotkov,[§] Lisa McElwee-White,[‡] and Timothy J. Anderson*[,†]

[†]Department of Chemical Engineering, University of Florida, Gainesville, Florida 32611-6005, United States

[‡]Department of Chemistry, University of Florida, Gainesville, Florida 32611-7200, United States

[§]Arkema Inc., 900 First Avenue, King of Prussia, Pennsylvania 19406, United States

Supporting Information

ABSTRACT: Aerosol-assisted chemical vapor deposition (AACVD) of WO_x was demonstrated using the oxo tungsten(VI) fluoroalkoxide single-source precursors, $WO[OCCH_3(CF_3)_2]_4$ and $WO[OC(CH_3)_2CF_3]_4$. Substoichiometric amorphous tungsten oxide thin films were grown on indium tin oxide (ITO) substrates in nitrogen at low deposition temperature (100−250 °C). At growth temperatures above 300 °C, the $W_{18}O_{49}$ monoclinic crystalline phase was observed. The surface morphology and roughness, visible light transmittance, electrical conductivity, and work function of the tungsten oxide materials are reported. The solvent and carrier gas minimally affected surface morphology and composition at low deposition temperature; however, material crystallinity varied with solvent choice at higher temperatures. The work function of the tungsten oxide thin films grown between 150 and 250 °C was determined to be in the range 5.0 to 5.7 eV, according to ultraviolet photoelectron spectroscopy (UPS).

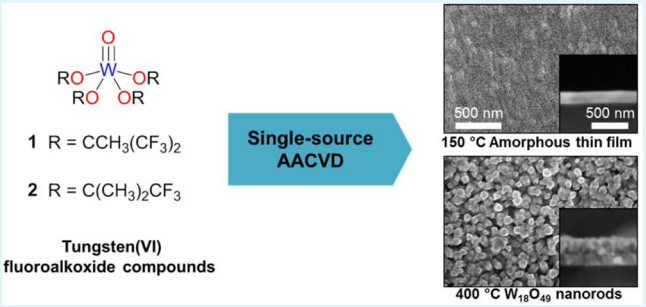

KEYWORDS: *tungsten oxide, nanorods, CVD, MOCVD, AACVD, tungsten oxo alkoxide compounds, OLED*

INTRODUCTION

Organic electronics, such as organic light emitting diodes (OLEDs) and organic photovoltaics (OPVs), utilize active organic materials made from naturally abundant resources. Therefore, they present the potential for a low cost, renewable, and green source of energy. Furthermore, the devices can be lightweight, mechanically flexible, and extremely thin,[1−4] which qualifies them for a wide range of applications. These devices have a sandwich structure that contains organic materials between an anode and cathode. The device configuration, however, can be complex, as the multilayer assembly comprises layers of different materials to enhance efficiency and reliability. For instance, in OLEDs, a hole-injection layer (HIL) is inserted between the anode and organic material to overcome the energy barrier existing at the interface and to increase hole transport efficiency.[1−5] Previous studies on HIL materials mostly concentrated on poly(3,4-ethylenedioxythiophene):poly(styrenesulfonate) (PEDOT:PSS).[2,3,6,7] This material, however, is limited by its work function of 5.0 eV, which is not sufficiently high to overcome the energy barrier between most relevant inorganic and organic materials.[8] Furthermore, PEDOT:PSS is highly acidic (pH 1.2). Studies on the device degradation patterns confirm that the sensitivity of the PEDOT:PSS layer to light and chemical reactions results in delamination from the organic emissive layer.[1,5,6] PEDOT:PSS is both hygroscopic and water reactive, which reduces its conductivity and device lifetime.[5,6,8]

Transition metal oxide HILs, such as MoO_3, NiO, V_2O_5, and WO_3, are receiving attention because they overcome these drawbacks.[7,9−11] Among the transition metal oxides, WO_x is most attractive because of its high work function (5.2−6.4 eV) and high visible light transparency, in addition to its mechanical, chemical, thermal, and electrical stability and robustness.[11−13] Moreover, WO_x can exist in multiple thermodynamic and Magnéli phases, each with a unique energy band structure.[14,15] Consequently, the work function, band gap, and other properties are tunable within a relatively wide range via stoichiometric and crystallographic control.[14,15] For instance, the substoichiometric phases of WO_{3-x} exhibit *n*-type semiconductor conductivity.[15] These adjustable properties favor HIL and a hole transport layer (HTL) applications.[16] A variety of growth techniques have been employed to synthesize

Received: November 5, 2014
Accepted: January 8, 2015
Published: January 8, 2015

DOI: 10.1021/am507706e
ACS Appl. Mater. Interfaces 2015, 7, 2660−2667

WO_x thin films, including direct heating of tungsten substrates in the presence of oxygen,[17] thermal evaporation of WO_3 powder,[18] vapor phase growth by heating a tungsten filament in oxidizing condition,[19] sputter deposition,[20] electrodeposition, and solution synthesis using precursors such as $W(CO)_6$, WCl_6, or WCl_4 in alcohol-based solutions.[21−23] Although some of these approaches to film deposition have served to provide a fundamental understanding of the structure and properties of WO_x materials, they can complicate device fabrication by requiring extremely high processing temperature or solution depositions, which may be detrimental to device components.[20] Chemical vapor deposition (CVD) is more compatible with current processing standards, because it has the capacity for in situ, large area and conformal growth at high throughput, and robust thin film growth of WO_x.[24−26] Additionally, CVD is typically operated under moderate processing conditions that reduce manufacturing cost.[27,28] In aerosol-assisted (AA)CVD, a precursor is transported in solution as a mist, and therefore, precursor volatility is less critical than in conventional CVD.[29] A somewhat common structural and morphological feature of substoichiometric CVD WO_x is the growth of nanorods.[30,31] Tungsten oxide nanorods also have several practical applications. For instance, WO_x nanorods on indium tin oxide (ITO) substrates show excellent field emission performance.[32] They are also used as anode materials in Li-ion secondary batteries to provide higher charge capacities and more stable discharge properties than bulk WO_3.[33] $W_{18}O_{49}$ nanorods on ITO exhibit high sensitivity and reversibility in detecting ultraviolet (UV) light.[34] In addition, porous substoichiometric tungsten oxide layers consisting of $W_{18}O_{49}$ nanorods show exceptional gas sensing characteristics due to their high surface area and numerous oxygen-deficient defects, which serve as adsorption sites.[35]

We now report AACVD growth of WO_x films and nanorods using the partially fluorinated oxo-alkoxide tungsten(VI) compounds, $WO[OCCH_3(CF_3)_2]_4$ (**1**) and $WO[OC(CH_3)_2CF_3]_4$ (**2**), as single-source precursors. The dependence of material properties on solvent and carrier gas has been explored.

EXPERIMENTAL DETAILS

Precursor Synthesis. The molecular single-source precursors $WO[OCCH_3(CF_3)_2]_4$ (**1**) and $WO[OC(CH_3)_2CF_3]_4$ (**2**) (Scheme 1) were synthesized as previously reported.[36]

Scheme 1. Synthesis of Precursors 1 and 2

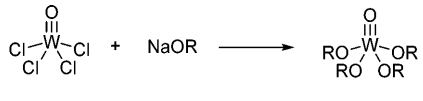

1 R = $CCH_3(CF_3)_2$
2 R = $C(CH_3)_2CF_3$

Tungsten Oxide Material Growth. Pure solid precursor was dissolved in anhydrous solvent (0.034 M) in a nitrogen-filled glovebox and then loaded into a gastight 10 mL syringe. Table S1 (Supporting Information) lists the physical properties of diglyme, benzonitrile, toluene, and dimethoxymethane (DME), solvents used for WO_x growth by AACVD. ITO (150 nm) coated borosilicate glass and bare borosilicate glass substrates were cleaned by sequential rinsing in boiling trichloroethylene, acetone, and methanol for 3 min each and then rinsed with boiling distilled water for 30 s to remove residual organic solvents. The prepared substrates were dried with nitrogen (99.999% purity, Airgas) before inserting them into the reactor. The reaction chamber was evacuated to at least 300 mTorr before purging for about 20 min and filling with N_2 carrier gas (99.999% purity, Airgas) or dry air at 350 Torr, maintained by a throttling valve downstream of the reaction chamber. Depositions using DME were operated at 700 Torr, to limit premature solvent vaporization. The carrier gas flow rate was maintained at 1000 sccm by a mass flow controller. The substrates were placed on a pedestal-type SiC coated graphite susceptor, and heated to the desired deposition temperature ranging from 100 to 400 °C by a radio frequency heat generator (Westinghouse). The precursor solution was then pumped into a nebulizer unit (U-5000AT, CETAC) by a syringe pump (EW-74900, Cole-Parmer) at a rate of 4 mL/h where it was converted to an aerosol solution by a piezoelectric quartz plate vibrating at 1.44 MHz. The aerosol was conveyed by the carrier gas through the heated (70 °C) precursor transport line and vertically impinging shower head jet. For all experiments the total film growth time was 150 min. A schematic of the reactor and more detailed description can be found elsewhere.[37]

Materials Characterization. X-ray photoelectron spectroscopy (XPS, PerkinElmer PHI 5100) with Al Kα radiation (hυ = 1486.3 eV) operating at 15 kV and 300 W was employed to measure the material composition and discern elemental valence states. To determine the effect of preferential sputtering, the surface of a sample at each growth temperature for precursor **1** was examined by XPS after Ar^+ sputtering for 0, 10, and 20 min. Without sputtering, XPS results revealed 18.0−30.8 at. % carbon contamination on the WO_x surface. After 10 min of sputtering (see Table S2, Supporting Information), half of the samples showed no carbon contamination and the other half showed minor carbon content (<3 at. %). After 20 min of sputtering, preferential O sputtering was observed, as more tungsten and less oxygen were detected. However, the W and O composition difference varied within a small range, 0.2−4.3 at. %. Thus, the samples were sputtered by 500 eV Ar^+ for 10 min to remove surface contaminants before XPS analyses. XPS measurements were performed in the range 1000 to 0 eV. Each sample was scanned 6 times and 10 swipes to compute the average surface composition and standard deviation. W 4f, O 1s, C 1s, In 3d, and Sn 3d peaks were checked to verify the material composition. No other atoms (e.g., F, N, and Si) were observed.

X-ray diffraction (XRD, Panalytical X'pert Pro) with monochromatized Cu Kα X-ray (λ = 1.5418 Å) source running at 45 kV and 40 mA was used to obtain crystallographic information. For thin films, grazing incidence X-ray diffraction (GIXD, Philips X'pert MRD) with a Cu Kα X-ray source, working at 45 kV and 40 mA, was used to maximize signal. The plan-view (surface morphology) and cross-sectional (film thickness) images of grown materials were taken by field emission scanning electron microscopy (FESEM, FEI Nova NanoSEM 430). The standard 5 kV acceleration voltage and a 5 mm working distance were adjusted to optimize image quality for some samples. The samples were examined by 2 × 2 μm area with 2 Hz scan rate via atomic force microscopy (AFM, Veeco Dimension 3100) to measure the film surface roughness. Transmittance in the range of 360 to 780 nm (visible light region) and conductivity were measured using an UV−vis spectroscopy (PerkinElmer Lambda 750) and a custom built 4-point probe, respectively. The work function and valence band structure of the films were measured by ultraviolet photoelectron spectroscopy (UPS, PerkinElmer PHI5000 Versa probe2) using a He^I (hυ = 21.22 eV) UV light source after Ar^+ sputtering the surface for 5 min.

RESULTS AND DISCUSSION

Precursor Choice. $WO[OCCH_3(CF_3)_2]_4$ (**1**) and $WO[OC(CH_3)_2CF_3]_4$ (**2**) (Scheme 1) were synthesized for delivery as single-source precursors in AACVD of WO_x materials.[36] AACVD requires precursor solubility and stability in organic solvents with suitable volatility. Compounds **1** and **2** form homogeneously stable solutions of an appropriate concentration in a wide range of solvents, especially ethereal solvents.[36] Additionally, **1** and **2** are sufficiently thermally stable for volatilization and transport without decomposition. This

DOI: 10.1021/am507706e
ACS Appl. Mater. Interfaces 2015, 7, 2660−2667

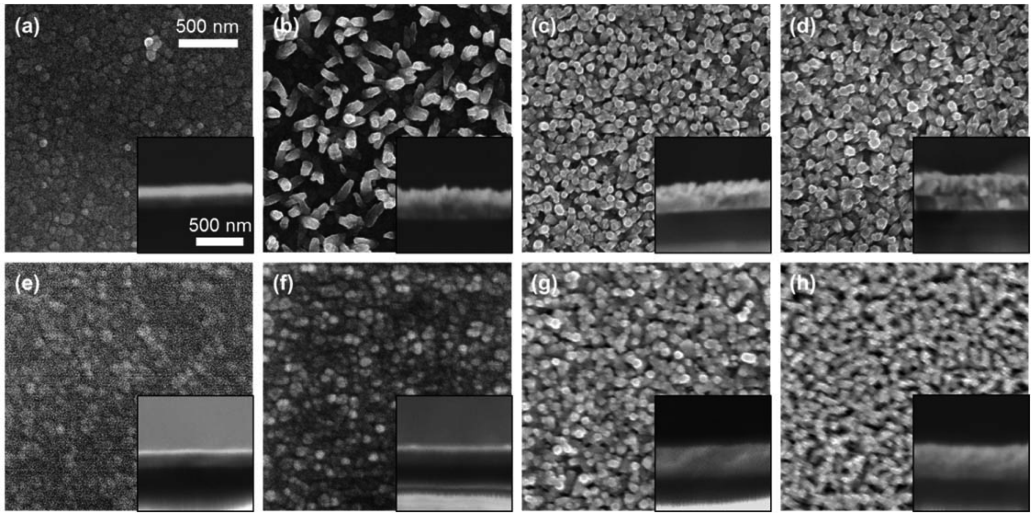

Figure 1. Plan-view and cross-sectional (inset) SEM images of materials grown with precursor **1** at (a) 250 °C, (b) 300 °C, (c) 350 °C, (d) 400 °C, and precursor **2** at (e) 250 °C, (f) 300 °C, (g) 350 °C, (h) 400 °C with diglyme and N_2 carrier gas.

was demonstrated by their sublimation at moderate temperatures and pressures (75−80 °C for **1** and 85−90 °C for **2** at 350−400 mTorr) with almost 100% recovery, while maintaining their respective yellowish and pale-yellowish solid appearances.[36] Compared with the well-known tungsten(VI) oxo-alkoxide/siloxide/phenoxide/salicylate precursors[38−40] that require substrate temperatures in excess of 400 °C or the polyoxotungstates,[41,42] exceeding 500 °C, selection of the tungsten(VI) oxo-fluoroalkoxide derivatives **1** and **2** as precursors permits further decrease in operational temperatures for growth of WO_x materials by AACVD, thus allowing access to a larger range of substrates and growth morphologies.

Tungsten Oxide Material Growth. Tungsten oxide films were grown in the temperature range 150−400 °C with **1** and in the range 250−400 °C with **2**. The plan-view SEM images in Figure 1 indicate that the deposited material exhibits two distinct morphologies depending on the growth temperature. The deposit produced from solutions of **1** at low deposition temperatures (≤250 °C) have thin film morphologies, whereas at 300 °C and higher, nanorod nucleation is observed. It appeared that low aspect ratio nanorods grew atop WO_x thin films between 350 and 400 °C, and above 450 °C, fully developed nanorods were present, as previously reported.[36] The morphology for WO_x grown from solutions of **2** evolved similarly, but with the nanorod nucleation evident in films grown at 350 and becoming fully developed at 400 °C. The change in deposited material morphology with growth temperature has not been previously reported. The shift in morphology occurs at relatively low temperatures and the transition temperature varied with the precursor, suggesting facile precursor decomposition is important.

The growth rates of materials were determined from deposit thickness measurements using cross-sectional SEM, as seen in Figure 1 insets. The films and nanorods grown at 150, 200, 250, 300, 350, and 400 °C from **1** exhibited film thickness or nanorod height of 22 (±6), 66 (±15), 82 (±13), 148 (±13), 180 (±10), and 265 (±22) nm, respectively. The growth rate dependence on the deposition temperature is shown in the Arrhenius plot in Figure 2. From the Arrhenius relationship, apparent activation energies (E_a) for growth are estimated at 0.22 (±0.02) eV and 0.34 (±0.02) eV for **1** and **2**, respectively. These values are lower than the typical kinetically controlled

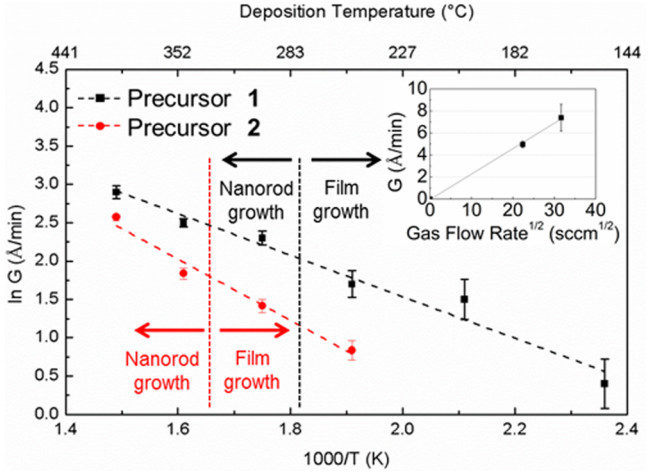

Figure 2. Arrhenius plot of growth rate vs inverse temperature for materials grown from precursors **1** and **2** (inset: growth rate dependence on the square root of the gas flow rate, for material grown with **1** at 300 °C).

growth (0.5 to 1 eV).[43] In addition, it was observed that the material growth rate was proportional to the square-root of the gas flow rate (see inset in Figure 2). This behavior along with the low apparent activation energies obtained from an Arrhenius plot is consistent with mass transport controlled deposition. From simple boundary layer theory the reactant flux, J, across the developed boundary layer to the surface is given by eq 1 and the boundary layer thickness, δ, for stagnation point flow is given by eq 2. Therefore, the reactant flux to the substrate surface and hence growth rate are proportional to the square-root of the reactant flow rate.[44−48]

$$J = \frac{D(p^* - p^i)}{RT\delta} \quad (1)$$

$$\delta = 2.4\sqrt{\frac{\mu L}{4U\rho}} \quad (2)$$

where D is the diffusion coefficient, p^* and p^i are the reactant partial pressure in the inlet and at the surface, R is the gas law constant, T is temperature, μ is the dynamic viscosity, L is the

DOI: 10.1021/am507706e
ACS Appl. Mater. Interfaces 2015, 7, 2660−2667

susceptor diameter, U is the stream velocity, and ρ is the fluid density.

As shown in Figure 3a, the tungsten atomic concentration in the films grown from **1** decreases from 33 to 27 at. % with

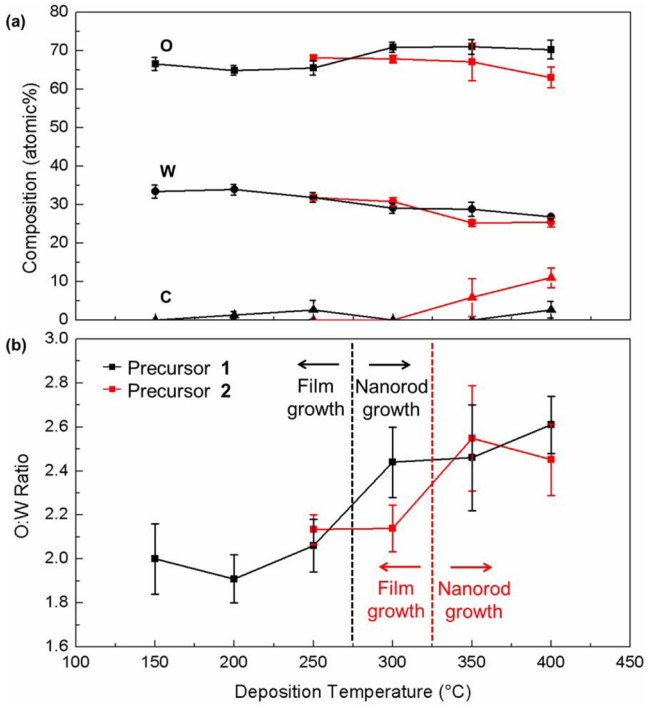

Figure 3. Comparison of (a) variation in elemental composition and (b) oxygen to tungsten atomic ratio (O:W) of materials grown with precursors **1** (black) and **2** (red).

increasing deposition temperature. Carbon impurities are minimally observed, with a maximum of only 3 at. % at the highest deposition temperature. The oxygen content increases slightly between 250 and 300 °C coinciding with the decrease of tungsten. Growth from **2** shows similar compositional patterns to those from **1**, but with greater carbon incorporation of 6 and 11 at. % at 350 and 400 °C, respectively (Table S2, Supporting Information). Possible sources of the increasing carbon content at high temperature include alternative precursor decomposition pathways, solvent decomposition, and an increase in surface bound carbon species upon morphological change from a film to nanorods.[36] It is noted that despite the presence of fluorinated ligands in both precursors, no fluorine was detected within the XPS instrument sensitivity limit of 1 at. %.

The W and O compositions and their ratio were determined from XPS measurements. A small In signal from the underlying ITO was detected for some samples due to the strong In $4d_{5/2}$ signal even for minor In levels (see Table S2, Supporting Information). The O level from the ITO substrate prior to deposition (59.4 at. % O, 37.6 at. % In, and 3.1 at. % Sn) was first subtracted. The compositional error was estimated as the standard deviation of values measured from the 6 scans per sample. The oxygen to tungsten (O:W) atomic ratio is plotted in Figure 3b and increases through the full range of deposition temperature and shows two apparent zones. Films grown from **1** and **2** at low temperatures (150−250 °C and 250−300 °C, respectively) have O:W ratios of approximately 2.0. In contrast, materials grown at relatively high temperatures exhibit O:W ratios varying from 2.4 to 2.6 for both precursors. This is consistent with W 4f peak binding energies (BEs) shifting from a lower value (34.9 eV at 200 °C) to a higher value (36.1 eV at 400 °C) (Figure S2, Supporting Information). The increase in the O:W ratio coincides with the onset of crystallinity at these temperatures, and an accompanying change in deposit morphology from amorphous film to nanorod nucleation and growth of monoclinic $W_{18}O_{49}$.

Figure 4 shows the effect of deposition temperature on the material crystallinity. Crystalline tungsten oxide has been

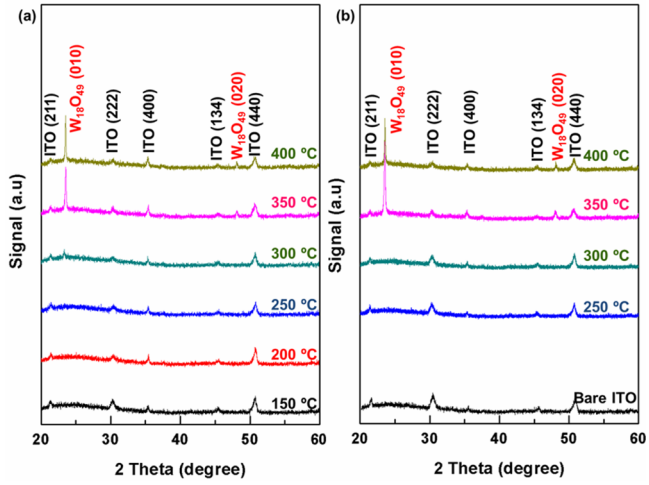

Figure 4. XRD patterns for materials grown with solutions of (a) **1** and (b) **2** at various deposition temperatures.

shown to perform better than amorphous material as a buffer layer because it has order promoted conductivity.[49,50] The materials grown from both precursors at deposition temperature greater than 300 °C exist in a tungsten oxide Magnéli phase; exhibiting diffraction peaks consistent with monoclinic $W_{18}O_{49}$. The diffraction peaks at 23.5 and 48.0° 2θ correspond to the (010) and (020) planes of monoclinic $W_{18}O_{49}$. This indicates that the preferred growth direction for the tungsten oxide nanorods is [010]. It has been reported that oxygen vacancies in the (010) plane of monoclinic $W_{18}O_{49}$ can lead to 1-D nanorod growth because precursors preferentially adsorb at these locally reduced surface sites.[51] Moreover, the [010] direction has the shortest interplanar spacing (lattice parameters for $W_{18}O_{49}$ monoclinic phase are a = 1.83, b = 0.38, and c = 1.4 nm). The Bravais−Friedel−Donnay−Harker (BFDH) law suggests the crystal face with the shortest interplanar space has the fastest growth rate, encouraging nanorod growth in that direction.[52,53] When solutions of **2** are used for growth, the WO_x material shows the same XRD reflections, but only at a slightly higher growth temperature (≥350 °C), which is consistent with the SEM images displayed in Figure 2. It should be noted that the broad amorphous hump present below 30 °2θ in the XRD spectra (Figure 4) corresponds to the amorphous borosilicate glass substrate beneath the ITO thin film. To verify the amorphous film microstructure, GIXD was employed (Figure S3, Supporting Information) and produced reflections corresponding to only the ITO substrate.

To use tungsten oxide as a HIL in OLED devices, surface work function, electrical conductivity, transparency, and surface roughness are important factors. A smoother buffer layer surface not only provides a more uniform conducting path for

DOI: 10.1021/am507706e
ACS Appl. Mater. Interfaces 2015, 7, 2660−2667

holes, but it also reduces series resistance across the interface due to carrier scattering and recombination.[54] The root-mean-square (RMS) surface roughness values acquired by AFM in Figure 5 qualitatively match the plan-view SEM images. The

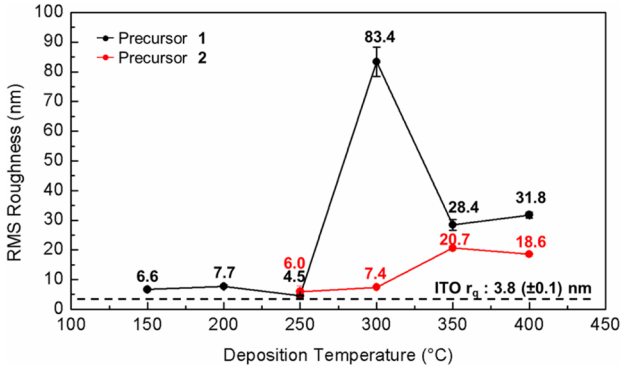

Figure 5. RMS surface roughness of grown materials as measured by AFM (dashed line indicates roughness of the ITO substrate).

deposit from **1** with film morphologies have RMS roughness values ranging from 4.5 (±0.2) to 7.7 (±0.4) nm. These values are slightly larger than the surface roughness (3.8 (±0.1) nm) of the ITO substrate. At 300 °C, the RMS value inflates to 83.4 (±5.0) nm, which is a product of the sparsely distributed nanorods on the surface (see Figure 2). The surface roughness decreases at 350 and 400 °C due to more uniformly distributed and closely packed short nanorods on the surface. The tungsten oxide materials grown at 250, and 300 °C using **2** show a relatively low surface roughness of 6.0 (±1.9) and 7.4 (±0.3) nm, respectively. Meanwhile, those grown at high temperature have rougher surfaces originating from nanorod growth.

The material transparency was measured by UV–vis spectroscopy. The samples grown on bare glass substrates at low temperatures (150 to 250 °C) are transparent and colorless. As the deposition temperature increases and the films become thicker, the samples become bluish and less transparent. The transmittance spectra in the range of 360 to 780 nm (visible region) of tungsten oxide deposited from **1** are presented in Figure 6. The tungsten oxide films grown at 150, 200, and 250 °C show mean transmittance values of 97, 90, and 86% in the visible region, respectively. The bluish samples grown at 350 and 400 °C show a maximum transmittance of

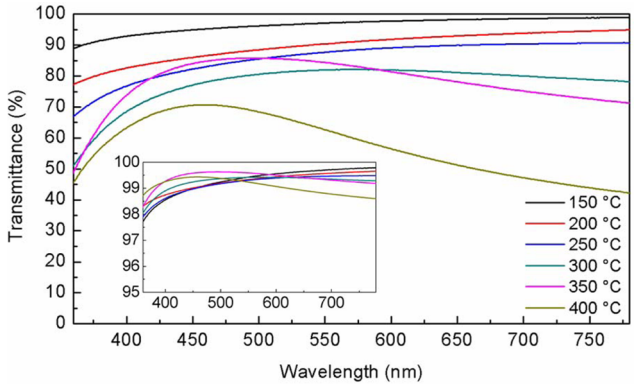

Figure 6. Transmittance of materials grown with precursor **1** at various values of deposition temperature (inset figure is normalized transmittance of 10 nm materials).

86% and 77% at a wavelength of 460 and 494 nm, respectively. This is consistent with other reports for $W_{18}O_{49}$ nanorods exhibiting blue emission, likely due to oxygen vacancies and quantum confinement effects.[1,4,55] The grown tungsten oxide materials show mean transmittance values higher than 99%, each when their thicknesses are normalized to 10 nm (see inset in Figure 6), the maximum required thickness for device structures.

The sheet resistance of samples was measured by the 4-point probe method, and then converted to conductivity. The tungsten oxide films deposited from **1** between 150 and 250 °C are highly resistive. As the material crystallizes to $W_{18}O_{49}$, its conductivity resembles that of a semiconductor. The conductivities of materials grown from 300, 350, and 400 °C are 0.12 (±0.01), 0.35 (±0.03), and 1.88 (±0.05) S/cm, respectively. $W_{18}O_{49}$ behaves as an *n*-type semiconductor with a conductivity reported as 2.58 S/cm for nanowire structures and 4 S/cm for bulk material.[56,57] These conductivities suggest that the deposit is a two-phase mixture of amorphous WO_x and monoclinic $W_{18}O_{49}$, with an increase in the amount of crystalline phase as the deposition temperature increases.

UPS was employed to measure the work function of films grown between 150 and 250 °C with precursor **1** on the ITO substrate. The measured work functions are 5.1, 5.0, and 5.7 eV for samples grown at 150, 200, and 250 °C, whereas the work function of the ITO substrate reference is 4.2 eV. These work functions are lower than the recently reported values for WO_3,[11,12] because the films grown from **1** and **2** are not fully oxidized and likely have oxygen defect energy states above the valence band. To overcome the energy barrier between an anode and an HTL in an OLED, a higher work function matching to the highest occupied molecular orbital (HOMO) level of the organic layer is preferred.[8]

Solvent and Carrier Gas Effect on Material Properties. Solvent properties may influence material properties in AACVD because the solvent can potentially participate in reactions, change delivery rates through solubility and volatilization differences, and modify mass transport characteristics. The growth studies were performed with four different solvents: diglyme, benzonitrile, DME, and toluene. Criteria for selection of solvents for AACVD are primarily based on precursor solubility and stability in solution, in addition to solvent volatility, surface tension, density, and viscosity for transport purposes. Experiments were also conducted with air as a carrier gas instead of nitrogen, in an effort to produce more stoichiometric films.

XPS atomic composition data for films grown with various solvents and the different carrier gas are illustrated in Figure 7. The chemical compositions for materials grown with benzonitrile and diglyme are very similar, despite their dissimilar properties. Materials grown with benzonitrile show no nitrogen incorporation and oxygen levels are similar to diglyme solvated precursors, which suggests that the solvent selection has minimal influence on the growth chemistry. In this deposition temperature range, materials deposited with diglyme and benzonitrile also show similar growth rate dependence on the deposition temperature, supporting the minimal solvent effect on growth (Figure S4, Supporting Information). With DME, tungsten oxide films could be grown at the lowest deposition temperature (100 °C) because higher operating pressure may increase the film growth rate. The materials grown at 350 °C with DME and toluene have O:W

DOI: 10.1021/am507706e
ACS Appl. Mater. Interfaces 2015, 7, 2660–2667

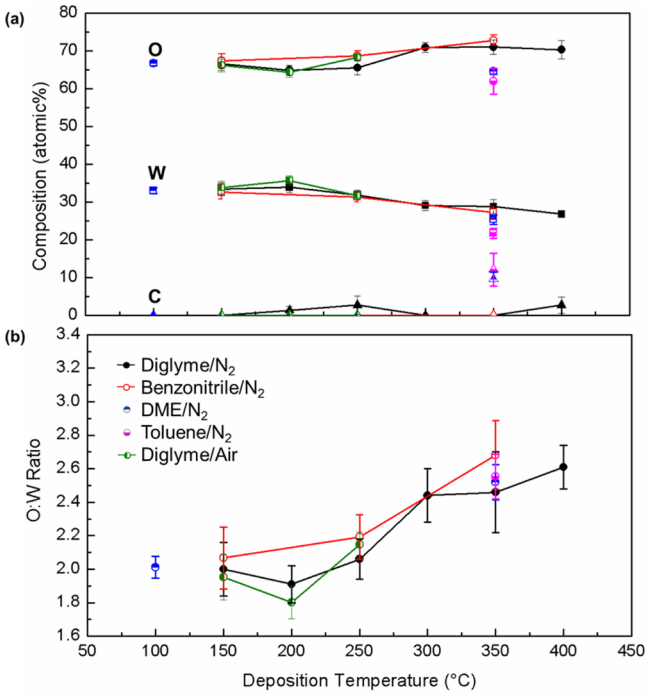

Figure 7. Comparison of (a) variation in chemical composition and (b) O:W ratio of materials grown from precursor **1** in different conditions.

ratios that are similar to materials grown with other solvents; however, they show about 10 at. % C impurity.

Using air as a carrier gas, substoichiometric tungsten oxide films were grown at low temperatures (≤250 °C), whereas only scattered particles formed at high temperatures (above 300 °C), likely due to upstream homogeneous reactions. According to energy-dispersive X-ray spectroscopy (EDS) analyses, the particles contain tungsten (Figure S5, Supporting Information). XPS data show no difference between materials grown with nitrogen and air, and the O:W ratio is nearly the same despite the additional oxygen source. This suggests that the film deposition is independent of the oxygen level in the carrier gas at low temperature, however at higher temperature there is sufficient energy available to overcome the energy barrier for gas-phase reactions.

The films grown at low temperature (≤250 °C) have no reflections corresponding to tungsten oxide, according to GIXD analyses, and appear to be completely amorphous regardless of solvent and carrier gas. In addition, UPS analysis shows that tungsten oxide films grown at 250 °C with different solvents and carrier gases have nearly the same work function of 5.7 eV. This suggests solvent and carrier gas have minimal effect on the tungsten oxide growth at low deposition temperature (Figure S6, Supporting Information).

Figure 8 shows plan-view SEM images of materials grown with benzonitrile, diglyme, toluene, and diglyme in dry air at selected temperatures. The surface morphologies are similar to that of material grown with diglyme in N_2. At low deposition temperatures (≤250 °C), thin film morphologies are observed, whereas at high temperatures (≥350 °C), the material consists of short nanorods.

In summary, changing the solvent appeared to have little to no influence on the structure and composition of the deposited materials, suggesting that the decomposition chemistry of precursors **1** and **2** determines the stoichiometry of the

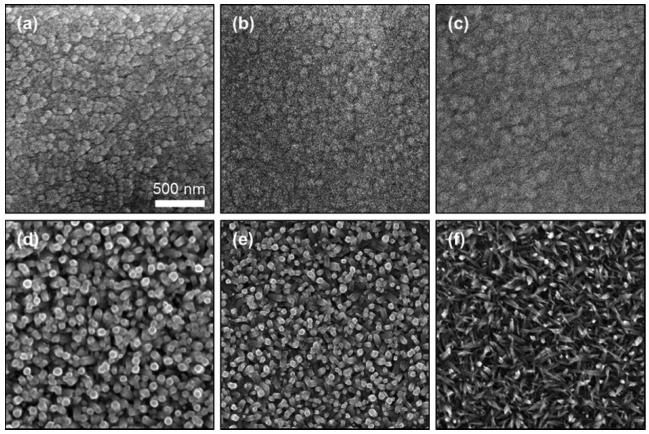

Figure 8. Plan-view SEM images of materials grown at (a) 100 °C with DME/N_2, (b) 250 °C with benzonitrile/N_2, (c) 250 °C with diglyme/air, (d) 350 °C with benzonitrile/N_2, (e) 350 °C with DME/N_2, and (f) 350 °C with toluene/N_2.

material. Solvent choice affected the XRD reflection intensities of nanorod growth, according to XRD measurements. It was observed that nanorods grown at 350 °C from **1** in benzonitrile display the most intense reflections (Figure 9). This

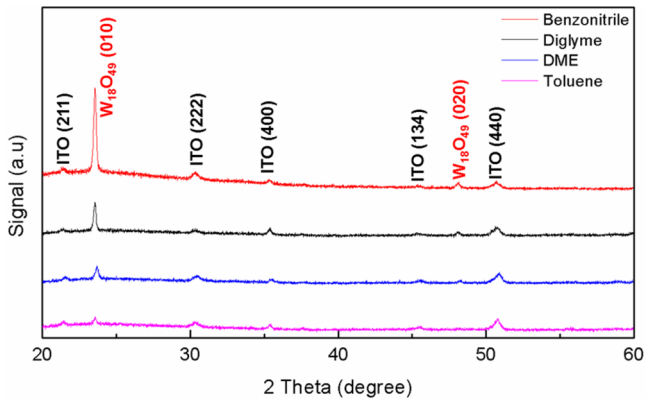

Figure 9. Comparison of XRD patterns of materials grown at 350 °C with various solvents.

observation seems to correlate well with the donor strengths, viscosity, and boiling points of the solvents. Toluene-based depositions exhibit the least amount of texturing. This may be due to toluene-based nanorod growth consisting of randomly oriented sharp tips, unlike materials grown with the other solvents (Figure 8f).

CONCLUSIONS

CVD has the capability to grow WO_x films of the precise thickness required for charge-injection applications in OLEDs and OPVs. AACVD of WO_x using the partially fluorinated oxo-alkoxide tungsten(VI) precursors **1** and **2** has been demonstrated to achieve facile growth of tungsten oxide thin films and nanorods on ITO and glass substrates. Substoichiometric amorphous thin films of WO_x ($2.0 < x < 2.3$) were grown at low deposition temperatures (≤250 °C). Between 300 and 350 °C, nanorod nucleation on amorphous films was observed, while short to fully developed tungsten oxide nanorod structures were grown above 400 °C. The O:W ratio increased with increasing deposition temperature, likely

DOI: 10.1021/am507706e
ACS Appl. Mater. Interfaces 2015, 7, 2660−2667

due to increased crystallinity. The hole-injection layer properties, such as surface roughness, transmittance, conductivity, and work function of tungsten oxide films were measured. The WO_x materials grown at low temperatures show a smooth surface, high visible light transmittance, and a higher work function than the ITO electrodes. Those properties are highly desirable for the thin buffer layers used in organic electronics. The properties of WO_x vary with stoichiometry and thus can be tuned to optimize the performance for a specific application. The work function varies directly with the value of x, with work function decreasing as the oxygen level decreases. In contrast, the relationship of electrical conductivity and x is inverse. Preliminary results suggest that the stoichiometry and crystallinity can be modified controllably by annealing. Solvent and carrier gas choice appeared to have a minimal effect on surface morphology and material composition. Crystallinity of the nanorods, however, was slightly dependent on the solvent, with benzonitrile encouraging the greatest crystallinity. Further growth studies and materials characterizations are underway to determine the nanorod nucleation and growth mechanism.

■ ASSOCIATED CONTENT

Supporting Information

(Table S1) Properties of solvents, (Table S2) XPS elemental composition, (Figure S1) additional SEM images, (Figure S2) XPS O 1s, C 1s, and W $4f_{5/2}$ and $4f_{7/2}$ peaks, (Figure S3) GIXD spectra, (Figure S4) Arrhenius plot of growth rate with different solvents and carrier gases, (Figure S5) EDS analysis results, and (Figure S6) UPS spectra. This material is available free of charge via the Internet at http://pubs.acs.org.

■ AUTHOR INFORMATION

Corresponding Author

*T. J. Anderson. E-mail: tim@ufl.edu.

Notes

The authors declare no competing financial interest.

■ ACKNOWLEDGMENTS

The authors thank the National Science Foundation for support under the GOALI grant CHE-1213965. We also thank the Major Analytical Instrumentation Center (MAIC) of the College of Engineering at the University of Florida for instrument instruction and maintenance, and particularly Eric Lambers for his assistance with UPS measurements.

■ REFERENCES

(1) Yella, A.; Tahir, M. N.; Meuer, S.; Zentel, R.; Berger, R.; Panthöfer, M.; Tremel, W. Synthesis, Characterization, and Hierarchical Organization of Tungsten Oxide Nanorods: Spreading Driven by Marangoni Flow. *J. Am. Chem. Soc.* **2009**, *131* (48), 17566−17575.

(2) Vasilopoulou, M.; Palilis, L. C.; Georgiadou, D. G.; Argitis, P.; Kennou, S.; Kostis, I.; Papadimitropoulos, G.; Stathopoulos, N. A.; Iliadis, A. A.; Konofaos, N.; Davazoglou, D.; Sygellou, L. Tungsten Oxides as Interfacial Layers for Improved Performance in Hybrid Optoelectronic Devices. *Thin Solid Films* **2011**, *519* (17), 5748−5753.

(3) Vasilopoulou, M.; Papadimitropoulos, G.; Palilis, L. C.; Georgiadou, D. G.; Argitis, P.; Kennou, S.; Kostis, I.; Vourdas, N.; Stathopoulos, N. A.; Davazoglou, D. High Performance Organic Light Emitting Diodes Using Substoichiometric Tungsten Oxide as Efficient Hole Injection Layer. *Org. Electron.* **2012**, *13* (5), 796−806.

(4) Xi, G.; Ouyang, S.; Li, P.; Ye, J.; Ma, Q.; Su, N.; Bai, H.; Wang, C. Ultrathin $W_{18}O_{49}$ Nanowires with Diameters below 1 nm: Synthesis, Near-Infrared Absorption, Photoluminescence, and Photochemical Reduction of Carbon Dioxide. *Angew. Chem., Int. Ed.* **2012**, *51* (10), 2395−2399.

(5) Schumann, S.; Da Campo, R.; Illy, B.; Cruickshank, A. C.; McLachlan, M. A.; Ryan, M. P.; Riley, D. J.; McComb, D. W.; Jones, T. S. Inverted Organic Photovoltaic Devices With High Efficiency and Stability Based on Metal Oxide Charge Extraction Layers. *J. Mater. Chem.* **2011**, *21* (7), 2381.

(6) Choi, H.; Kim, B.; Ko, M. J.; Lee, D. K.; Kim, H.; Kim, S. H.; Kim, K. Solution Processed WO_3 layer for the Replacement of PEDOT:PSS Layer in Organic Photovoltaic Cells. *Org. Electron.* **2012**, *13* (6), 959−968.

(7) Meyer, J.; Hamwi, S.; Kroger, M.; Kowalsky, W.; Riedl, T.; Kahn, A. Transition Metal Oxides for Organic Electronics: Energetics, Device Physics and Applications. *Adv. Mater.* **2012**, *24* (40), 5408−5427.

(8) Choudhury, K. R.; Lee, J. W.; Chopra, N.; Gupta, A.; Jiang, X. Z.; Amy, F.; So, F. Highly Efficient Hole Injection Using Polymeric Anode Materials for Small-Molecule Organic Light-Emitting Diodes. *Adv. Funct. Mater.* **2009**, *19* (3), 491−496.

(9) Xie, G. H.; Meng, Y. L.; Wu, F. M.; Tao, C.; Zhang, D. D.; Liu, M. J.; Xue, Q.; Chen, W.; Zhao, Y. Very Low Turn-On Voltage and High Brightness Tris(8-hydroxyquinoline)aluminum-based Organic Light-Emitting Diodes With a MoO_x p-Doping Layer. *Appl. Phys. Lett.* **2008**, *93* (22), 229902.

(10) Chan, I. M.; Hsu, T. Y.; Hong, F. C. Enhanced Hole Injections in Organic Light-Emitting Devices by Depositing Nickel Oxide on Indium Tin Oxide Anode. *Appl. Phys. Lett.* **2002**, *81* (10), 1899−1901.

(11) Son, M. J.; Kim, S.; Kwon, S.; Kim, J. W. Interface Electronic Structures of Organic Light-Emitting Diodes with WO_3 Interlayer: A Study by Photoelectron Spectroscopy. *Org. Electron.* **2009**, *10* (4), 637−642.

(12) Ryland, B. L.; Stahl, S. S. Practical Aerobic Oxidations of Alcohols and Amines with Homogeneous Copper/TEMPO and Related Catalyst Systems. *Angew. Chem., Int. Ed.* **2014**, *53*, 8824−8838.

(13) Vida, G.; Josepovits, V. K.; Gyor, M.; Deak, P. Characterization of Tungsten Surfaces by Simultaneous Work Function and Secondary Electron Emission Measurements. *Microsc. Microanal.* **2003**, *9* (4), 337−342.

(14) Migas, D. B.; Shaposhnikov, V. L.; Rodin, V. N.; Borisenko, V. E.; Tungsten Oxides, I. Effects of Oxygen Vacancies and Doping on Electronic and Optical Properties of Different Phases of WO_3. *J. Appl. Phys.* **2010**, *108* (9), 093713.

(15) Migas, D. B.; Shaposhnikov, V. L.; Borisenko, V. E. Tungsten Oxides. II. The Metallic Nature of Magneli Phases. *J. Appl. Phys.* **2010**, *108* (9), 093714.

(16) Acharya, R.; Cao, X. A. High-Brightness Organic Light-Emitting Diodes Based on a Simplified Hybrid Structure. *Appl. Phys. Lett.* **2012**, *101* (5), 053306.

(17) Liu, Z.; Bando, Y.; Tang, C. Synthesis of Tungsten Oxide Nanowires. *Chem. Phys. Lett.* **2003**, *372* (1−2), 179−182.

(18) Baek, Y.; Yong, K. Controlled Growth and Characterization of Tungsten Oxide Nanowires Using Thermal Evaporation of WO_3 Powder. *J. Phys. Chem. C* **2007**, *111* (3), 1213−1218.

(19) Vaddiraju, S.; Chandrasekaran, H.; Sunkara, M. K. Vapor Phase Synthesis of Tungsten Nanowires. *J. Am. Chem. Soc.* **2003**, *125* (36), 10792−10793.

(20) Chen, C.-H.; Wang, S.-J.; Ko, R.-M.; Kuo, Y.-C.; Uang, K.-M.; Chen, T.-M.; Bor-Wen, L.; Tsai, H.-Y. The Influence of Oxygen Content in the Sputtering Gas on the Self-Synthesis of Tungsten Oxide Nanowires on Sputter-Deposited Tungsten Films. *Nanotechnology* **2006**, *17* (1), 217.

(21) Woo, K.; Hong, J.; Ahn, J. P.; Park, J. K.; Kim, K. J. Coordinatively Induced Length Control and Photoluminescence of $W_{18}O_{49}$ Nanorods. *Inorg. Chem.* **2005**, *44* (20), 7171−7174.

(22) Polleux, J.; Pinna, N.; Antonietti, M.; Niederberger, M. Growth and Assembly of Crystalline Tungsten Oxide Nanostructures Assisted by Bioligation. *J. Am. Chem. Soc.* **2005**, *127* (44), 15595−15601.

(23) Seo, J.-w.; Jun, Y.-w.; Ko, S. J.; Cheon, J. In Situ One-Pot Synthesis of 1-Dimensional Transition Metal Oxide Nanocrystals. *J. Phys. Chem. B* **2005**, *109* (12), 5389−5391.

DOI: 10.1021/am507706e
ACS Appl. Mater. Interfaces 2015, 7, 2660−2667

(24) Palgrave, R. G.; Parkin, I. P. Chemical Vapor Deposition of Titanium Chalcogenides and Pnictides and Tungsten Oxide Thin Films. *New J. Chem.* **2006**, *30* (4), 505−514.
(25) McElwee-White, L. Design of Precursors for the CVD of Inorganic Thin Films. *Dalton Trans.* **2006**, 5327−5333.
(26) Kirss, R. U.; Meda, L. Chemical Vapor Deposition of Tungsten Oxide. *Appl. Organomet. Chem.* **1998**, *12* (3), 155−160.
(27) Ma, X.; Starke, K.; Schulzke, C.; Schmidt, H.-G.; Noltemeyer, M. Structural, Electrochemical, and Theoretical Investigations of New Thio- and Selenoether Complexes of Molybdenum and Tungsten. *Eur. J. Inorg. Chem.* **2006**, No. 3, 628−637.
(28) Thapper, A.; Balmes, O.; Lorber, C.; Svensson, P. H.; Holm, R. H.; Nordlander, E. Synthesis and Structural Characterization of Two Tungsten(VI) Dioxo Complexes with *N,O*- and *N,S*-coordinating Ligands. *Inorg. Chim. Acta* **2001**, *321* (1,2), 162−166.
(29) Hubert-Pfalzgraf, L. G.; Guillon, H. Trends in Precursor Design for Conventional and Aerosol-Assisted CVD of High-Tc Superconductors. *Appl. Organomet. Chem.* **1998**, *12* (3), 221−236.
(30) Klinke, C.; Hannon, J. B.; Gignac, L.; Reuter, K.; Avouris, P. Tungsten Oxide Nanowire Growth by Chemically Induced Strain. *J. Phys. Chem. B* **2005**, *109* (38), 17787−17790.
(31) Mitra, S.; Sridharan, K.; Unnam, J.; Ghosh, K. Synthesis of Nanometal Oxides and Nanometals Using Hot-wire and Thermal CVD. *Thin Solid Films* **2008**, *516* (5), 798−802.
(32) Huang, K.; Pan, Q. T.; Yang, F.; Ni, S. B.; He, D. Y. Growth and Field Emission of Tungsten Oxide Nanotip Arrays on ITO Glass Substrate. *Appl. Surf. Sci.* **2007**, *253* (22), 8923−8927.
(33) Huang, K.; Pan, Q.; Yang, F.; Ni, S.; Wei, X.; He, D. Controllable Synthesis of Hexagonal WO_3 Nanostructures and their Application in Lithium Batteries. *J. Phys. D: Appl. Phys.* **2008**, *41* (15), 155417.
(34) Yang, F.; Huang, K.; Ni, S.; Wang, Q.; He, D. $W_{18}O_{49}$ Nanowires as Ultraviolet Photodetector. *Nanoscale Res. Lett.* **2010**, *5* (2), 416−419.
(35) Kim, Y. S.; Ha, S.-C.; Kim, K.; Yang, H.; Choi, S.-Y.; Kim, Y. T.; Park, J. T.; Lee, C. H.; Choi, J.; Paek, J.; Lee, K. Room-Temperature Semiconductor Gas Sensor Based on Nonstoichiometric Tungsten Oxide Nanorod Film. *Appl. Phys. Lett.* **2005**, *86* (21), 213105.
(36) Bonsu, R. O.; Kim, H.; O'Donohue, C.; Korotkov, R. Y.; McClain, K. R.; Abboud, K. A.; Ellsworth, A. A.; Walker, A. V.; Anderson, T. J.; McElwee-White, L. Partially Fluorinated Oxo-Alkoxide Tungsten(VI) Complexes as Precursors for Deposition of WO_x Nanomaterials. *Dalton Trans.* **2014**, *43* (24), 9226−9233.
(37) McClain, K. R.; O'Donohue, C.; Shi, Z.; Walker, A. V.; Abboud, K. A.; Anderson, T.; McElwee-White, L. Synthesis of $WN(NMe_2)_3$ as a Precursor for the Deposition of WNx Nanospheres. *Eur. J. Inorg. Chem.* **2012**, *2012* (29), 4579−4584.
(38) Basato, M.; Brescacin, E.; Tondello, E. Amorphous WO_3 films via "wet" CVD of a W(VI) Oxoalkoxide Precursor. *Chem. Vap. Deposition* **2001**, *7* (5), 219−224.
(39) Cross, W. B.; Parkin, I. P.; O'Neill, S. A.; Williams, P. A.; Mahon, M. F.; Molloy, K. C. Tungsten Oxide Coatings from the Aerosol-Assisted Chemical Vapor Deposition of $W(OAr)_6$ (Ar = C_6H_5, C_6H_4F-4, $C_6H_3F_2$-3,4); Photocatalytically Active γ-WO_3 Films. *Chem. Mater.* **2003**, *15* (14), 2786−2796.
(40) Cross, W. B.; Parkin, I. P.; White, A. J. P.; Williams, D. J. Synthesis and Characterization of Tungsten(VI) Oxo-Salicylate Complexes for Use in the Chemical Vapor Deposition of Self-Cleaning Films. *Dalton Trans.* **2005**, No. 7, 1287−1293.
(41) Cross, W. B.; Parkin, I. P. Aerosol Assisted Chemical Vapor Deposition of Tungsten Oxide Films from Polyoxotungstate Precursors: Active Photocatalysts. *Chem. Commun.* **2003**, No. 14, 1696−1697.
(42) Ashraf, S.; Blackman, C. S.; Palgrave, R. G.; Parkin, I. P. Aerosol-Assisted Chemical Vapor Deposition of WO_3 Thin Films Using Polyoxometalate Precursors and Their Gas Sensing Properties. *J. Mater. Chem.* **2007**, *17* (11), 1063−1070.
(43) Raaijmakers, I. J.; Yang, J. Low-Temperature MOCVD of Advanced Barrier Layers for the Microelectronics Industry. *Appl. Surf. Sci.* **1993**, *73*, 31−41.
(44) White, F. M. *Viscous Fluid Flow*, Second ed.; McGraw-Hill Inc.: New York, 1991; p 614.
(45) Eversteyn, F. C.; Severin, P. J. W.; Brekel, C. H. J. v. d.; Peek, H. L. A Stagnant Layer Model for Epitaxial Growth of Silicon From Silane in a Horizontal Reactor. *J. Electrochem. Soc.* **1970**, *117* (7), 925−931.
(46) Stringfellow, G. B. Organometallic Vapor-Phase Epitaxial-Growth of III-V Semiconductors. *Semicond. Semimetals* **1985**, *22*, 209−259.
(47) Kim, M. S.; Chun, J. S. Effects of the Experimental Conditions of Chemical Vapor-Deposition on a TiC/TiN Double-Layer Coating. *Thin Solid Films* **1983**, *107* (2), 129−139.
(48) Heinecke, H.; Veuhoff, E.; Putz, N.; Heyen, M.; Balk, P. Kinetics of GaAs Growth by Low-Pressure MO-CVD. *J. Electron. Mater.* **1984**, *13* (5), 815−830.
(49) Li, J.; Yahiro, M.; Ishida, K.; Yamada, H.; Matsushige, K. Enhanced Performance of Organic Light Emitting Device by Insertion of Conducting/Insulating WO_3 Anodic Buffer Layer. *Synth. Met.* **2005**, *151* (2), 141−146.
(50) Miyake, K.; Kaneko, H.; Sano, M.; Suedomi, N. Physical and Electrochromic Properties of the Amorphous and Crystalline Tungsten Oxide Thick Films Prepared Under Reducing Atmosphere. *J. Appl. Phys.* **1984**, *55* (7), 2747−2753.
(51) Smith, A. M.; Kast, M. G.; Nail, B. A.; Aloni, S.; Boettcher, S. W. Planar-Defect-Driven Growth Mechanism of Oxygen Deficient Tungsten Oxide Nanowires. *J. Mater. Chem. A* **2014**, *2*, 6121−6129.
(52) Frey, G. L.; Rothschild, A.; Sloan, J.; Rosentsveig, R.; Popovitz-Biro, R.; Tenne, R. Investigations of Nonstoichiometric Tungsten Oxide Nanoparticles. *J. Solid State Chem.* **2001**, *162* (2), 300−314.
(53) Donnay, J. D. H.; Harker, D. A New Law of Crystal Morphology Extending the Law of Bravais. *Am. Mineral.* **1937**, *22* (5), 446−467.
(54) Chen, S. F.; Wang, C. W. Influence of the Hole Injection Layer on the Luminescent Performance of Organic Light-Emitting Diodes. *Appl. Phys. Lett.* **2004**, *85* (5), 765−767.
(55) Chen, Z.; Wang, Q.; Wang, H.; Zhang, L.; Song, G.; Song, L.; Hu, J.; Wang, H.; Liu, J.; Zhu, M.; Zhao, D. Ultrathin PEGylated $W_{18}O_{49}$ Nanowires as a New 980 nm-Laser-Driven Photothermal Agent for Efficient Ablation of Cancer Cells in Vivo. *Adv. Mater.* **2013**, *25* (14), 2095−2100.
(56) Salje, E.; Güttler, B. Anderson Transition and Intermediate Polaron Formation in WO_{3-x} Transport Properties and Optical Absorption. *Philos. Mag. B* **1984**, *50* (5), 607−620.
(57) Shi, S.; Xue, X.; Feng, P.; Liu, Y.; Zhao, H.; Wang, T. Low-temperature Synthesis and Electrical Transport Properties of $W_{18}O_{49}$ Nanowires. *J. Cryst. Growth* **2008**, *310* (2), 462−466.

DOI: 10.1021/am507706e
ACS Appl. Mater. Interfaces 2015, 7, 2660−2667